

L. F. Kallivokas · S. Lee

Ellipsoidally-shaped local absorbing boundaries for three-dimensional scalar wave propagation

Received: 1 September 2003 / Accepted: 13 April 2004 / Published online: 22 September 2004
© Springer-Verlag 2004

Abstract In this paper we discuss the performance of second-order absorbing conditions prescribed on ellipsoidally-shaped truncation boundaries for the resolution of scalar wave phenomena in three dimensions. The second-order conditions employed herein belong to a larger class of arbitrarily-shaped convex absorbing boundaries developed earlier [21] for acoustic scattering and radiation problems in unbounded domains. In [21] we discussed their performance when used on spherical truncation boundaries for applications in both the time- and frequency-domains. Here, we extend their applicability to ellipsoidal geometries and demonstrate that significant computational savings are attainable due to the reduced computational domain afforded by the ellipsoid.

1 Introduction

In a plethora of practical engineering problems there is need to resolve the propagation of acoustic waves in unbounded domains. Problems of interest involving the study of acoustic scattering and radiation phenomena typically arise in underwater acoustics, in fluid-structure interaction, in target-identification problems, and in the noise-control industry.

Invariably, such problems involve scatterers embedded in a wave-supporting unbounded medium; the

primary challenge in the numerical modeling of the propagating waves is rooted in the infinite extent of the host medium. If domain discretization methods are used, the unbounded domain must be replaced by a finite computational domain that results when a truncation boundary limits the infinite extent of the original domain. For well-posedness of the ensuing mathematical problem, an appropriate boundary condition need accompany the introduction of the truncation boundary (see e.g., [19] for a recent review). The condition can be seen as a near-field instantiation (as opposed to at-infinity) of the Sommerfeld radiation condition. Such a condition is exact, referred to as the DtN map (see [16, 17] for reviews of exact treatments), for it relates the Dirichlet with the Neumann datum on the truncation boundary; it is, however, non-local in both space and time. Local approximants of the DtN map that relax the spatial, or the temporal non-locality, or both, are capable of reducing the computational cost associated with non-local conditions, albeit at the expense of accuracy.

Local conditions are desirable even in frequency-domain applications where the boundary element method has been long-dominant: despite the advantage integral equations offer in accurately treating the unbounded medium via the embedded Green's functions, at the high-frequency regime the resulting dense algebraic systems will exact even advanced modern-day hardware architectures for applications in three dimensions.

Overcoming the computational cost associated with boundary integral formulations, infinite elements, an approach pioneered by Bettess and Zienkiewicz [8, 9], offer a competitive alternative in the context of domain methods. The central idea in infinite elements is to allow for asymptotic expansions of the solution exterior to the truncation boundary in the (outwardly) radial direction. Finite elements incorporating, via appropriately constructed shape functions, radial expansions of variable order can then be prescribed on the truncation boundary. Implementations of infinite element ideas in

L. F. Kallivokas (✉)
Department of Civil Engineering,
The University of Texas, Austin,
TX 78712, USA
E-mail: loukas@mail.utexas.edu,
Tel.: 512-232-5769
Fax: 512-471-7259

S. Lee
Department of Civil Engineering,
The University of Texas, Austin,
TX 78712, USA
E-mail: sang@mail.utexas.edu

acoustics, particular to canonical truncation geometries (prolate and oblate spheroidal and ellipsoidal), have been implemented by Burnett [11, 12]. However, their application is limited to the frequency domain; moreover, recent studies on the convergence of infinite element formulations [2–4, 25] reveal difficulties with the conditioning of the resulting algebraic systems.

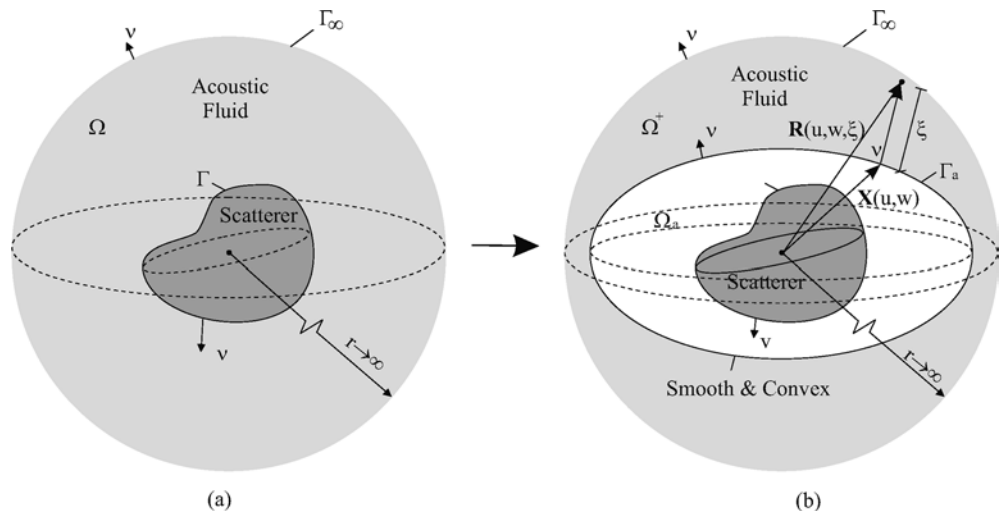
An early modification to infinite elements [7] was due to Astley’s novel idea of allowing the test functions to be (weighted) complex conjugates of the trial functions, in the context of Galerkin finite elements (see [24] for a theoretical justification). The approach gave rise to the so-called wave-envelope elements (see [4] for an overview), that are closely related to the more recent “conjugated” infinite element formulations [15]. Whereas wave-envelope elements are not immune to the aforementioned conditioning difficulty, the problem can be alleviated by a judicious choice of the radial basis [4]. The choice of complex conjugates for the test and trial functions is a significant one, for it endows the wave-envelope elements with the capability to tackle transient applications [5, 6], contrary to most infinite element formulations. Still, whether conjugated or unconjugated, infinite or wave-envelope elements, with or without conditioning difficulties, such “infinite” element formulations are captive to the particular coordinate system for which the radial expansions were originally written.

Similarly dependent on the coordinate system are the very few efforts to derive exact (DtN) conditions at a truncation boundary that is neither circular or spherical. For example, in [18] the authors derived DtN maps for elliptical and spheroidal boundaries. Implementations of these conditions in the context of finite elements appeared later in [27]. However, the conditions, by construction, remain non-local, entailing the computational difficulties alluded to earlier. Thus, for the computational advantages local conditions offer over non-local boundary treatments, and for the ease by

which they can be coupled with domain methods, in this work we favor local absorbing conditions and report on the performance of ellipsoidally-shaped boundaries. The work builds on earlier developments: in [21] we presented a procedure for constructing a family of absorbing boundary conditions for three-dimensional truncation geometries, which, to the best of our knowledge, were the first to be *systematically* developed for arbitrarily-convex boundary shapes. Earlier systematic developments include the works of Engquist and Majda, and Bayliss and Turkel [10, 13, 14]; the local conditions derived in these works were however limited to canonical geometries. In [20], Jones developed a three-dimensional second-order condition for general convex geometries by extending to three dimensions a two-dimensional condition developed earlier by Kriegsmann [23], who in turn used an *ad-hoc* procedure for extending the Bayliss and Turkel conditions [10] to arbitrarily convex geometries. Jones in [20], used the three-dimensional condition as an on-surface radiation condition; however, in [21, 22] we showed that the condition was not stable for time-domain applications and sub-optimal for frequency-domain applications.

More recently, Antoine et al. [1], using pseudo-differential calculus, developed a second-order condition for arbitrarily-convex absorbing boundaries and applied it as an on-surface condition in the frequency-domain only; our own conditions are, in some cases, (e.g., condition of order $\frac{3}{2}$ in [1]) reducible to their conditions. In [26] the authors used the second-order condition of Antoine et al. in the context of a finite element formulation and presented results for ellipsoidal boundaries in the frequency-domain. In this paper, we use the conditions we had developed earlier [21] and particularize them to ellipsoidally-shaped boundaries in both the frequency- and the time-domains: we show that significant computational gains are attainable when ellipsoidal boundaries are used over spherical, without a significant loss of accuracy.

Fig. 1 **a** Model of scatterer embedded in an unbounded acoustic fluid Ω , **b** model with finite computational domain Ω_a and absorbing boundary Γ_a



2 Exterior problem – strong form statement

We are concerned with the initial-and-boundary value problem (IBVP) associated with the time-dependent scalar wave equation in an unbounded domain. Let Γ be a closed surface with exterior $\Omega \subset \mathbb{R}^3$; Ω is occupied by a linear, inviscid, and compressible fluid (Fig. 1a). Without loss of generality we consider the radiation problem in which Γ is subjected to a prescribed acceleration field¹. Then the strong form becomes: find $p(\mathbf{x}, t)$ such that:

$$\ddot{p}(\mathbf{x}, t) = c^2 \Delta p(\mathbf{x}, t), \mathbf{x} \in \Omega, \quad t \geq 0, \quad (1)$$

$$p_v(\mathbf{x}, t) = f_N(\mathbf{x}, t), \mathbf{x} \in \Gamma, \quad t > 0 \quad (2)$$

$$\lim_{r \rightarrow \infty} r(p_r + \frac{1}{c}\dot{p}) = 0, \quad \text{and} \quad (3)$$

$$p(\mathbf{x}, 0) = 0, \dot{p}(\mathbf{x}, 0) = 0, \mathbf{x} \in \bar{\Omega}, \quad (4)$$

where p denotes pressure; \mathbf{x} is the position vector, t is time; v is the outward unit normal on Γ ; c is the velocity of wave propagation; p_v denotes the normal derivative of the pressure p ; Δ is the Laplace operator; an overdot denotes derivative with respect to time; an overbar denotes closure; and f_N is a prescribed function. Condition (3), in which r is radial distance and p_r the derivative of the pressure along the radial direction, is the Sommerfeld radiation condition. Condition (4) indicates that the system is taken to be initially at rest.

Next, to resolve the propagating waves within Ω using domain discretization methods, one needs to truncate the exterior region by introducing an artificial boundary Γ_a , as shown in Fig. 1b. This truncation gives rise to a bounded subdomain Ω_a (with exterior the unbounded Ω^+). In order for the solution p to coincide with that of the original problem within the truncated region Ω_a , it is necessary to specify a boundary condition on Γ_a that will ensure that the outgoing waves crossing Γ_a are undisturbed by the presence of this boundary. This boundary condition, which can be determined in terms of the actual solution p on Γ_a is of the form:

$$p_v(\mathbf{x}, t) = \mathcal{F}[p^t(\cdot, \cdot)](\mathbf{x}), \quad \mathbf{x} \in \Gamma_a, \quad (5)$$

where the dots following p^t indicate dummy variables, and \mathcal{F} is a pseudo-differential operator that depends on p^t , the time history of p , i.e.,

$$p^t(t) = p(t - \tau), \quad \forall \tau: 0 \leq \tau \leq t. \quad (6)$$

The operator \mathcal{F} captures symbolically the exact form of the DtN map needed for well-posedness of the resulting IBVP over the (now) truncated computational domain Ω_a . \mathcal{F} , however, is non-local in time and space, that is to

say, the motion at any given instant t at every point on the artificial boundary Γ_a is coupled with the time histories of all other points on Γ_a . The non-local character of the exact \mathcal{F} makes it unsuitable for implementation in the context of domain methods. Herein, as shown later, we employ a localized approximant to \mathcal{F} that is particularly well-suited for numerical implementation using finite elements.

3 The Absorbing Boundary

In [21], a family of localized approximants to the exact pseudo-differential operator \mathcal{F} for arbitrarily-convex truncation boundaries Γ_a was developed, and its members were used in applications involving spherical truncation boundaries. The development in [21] was based on high-frequency asymptotic expansions in the Laplace-transform domain inspired by geometrical optics ideas. Herein, we use a second-order² approximant to \mathcal{F} , henceforth denoted by \mathcal{F}_2 , prescribed on ellipsoidal or (its degenerate counterparts) spheroidal boundaries. In [21], to accommodate the arbitrary geometry we introduced a new coordinate system in $\bar{\Omega}^+$: if Γ_a is described by the parametric representation $\mathbf{X}(u, w)$ where \mathbf{X} denotes the position vector on Γ_a , and u, w are the surface parameters, then a new coordinate system is introduced by the description:

$$\mathbf{R}(u, w, \xi) = \mathbf{X}(u, w) + \xi v(u, w), \quad \xi \geq 0, \quad (7)$$

where \mathbf{R} denotes position vector in Ω^+ , ξ is a scalar, and v is the outward normal to Γ_a (Fig. 1b). Since Γ_a is convex and smooth, the new system is global in Ω^+ . Notice that for $\xi = 0$, (7) provides the parametric representation of Γ_a . Using this coordinate system, the second-order local approximant to the operator symbol in (5) is [21]: first, in the frequency-domain (a caret over a variable denotes its Laplace-transformed counterpart³):

$$\begin{aligned} \hat{p}_v = \hat{\mathcal{F}}_2[\hat{p}] = & -\frac{s}{c}\hat{p} + H\hat{p} + \frac{c}{2(s+\gamma)} \\ & + \left\{ \frac{1}{\sqrt{h}} \left\{ \left[\frac{1}{\sqrt{h}} (h_{22}\hat{p}_u - h_{12}\hat{p}_w) \right]_u \right. \right. \\ & \left. \left. + \left[\frac{1}{\sqrt{h}} (-h_{12}\hat{p}_u + h_{11}\hat{p}_w) \right]_w \right\} \right. \\ & \left. + (H^2 - K)\hat{p} \right\}, \quad (8) \end{aligned}$$

where $\hat{\mathcal{F}}_2$ denotes the approximate functional of second-order. Translation of (8) back to the time-domain yields:

²Second-order with respect to frequency, i.e., the second-order condition is $O(s^{-2})$, with s denoting frequency.

³With $s = i\omega$, where ω denotes circular frequency.

¹Scattering problems are similarly treated.

$$\begin{aligned}
\dot{p}_v + \gamma p_v = & -\frac{1}{c}\ddot{p} + \left(H - \frac{\gamma}{c}\right)\dot{p} + H\gamma p \\
& + \frac{c}{2} \left\{ \frac{1}{\sqrt{h}} \left\{ \left[\frac{1}{\sqrt{h}} (h_{22}p_u - h_{12}p_w) \right]_u \right. \right. \\
& \quad \left. \left. + \left[\frac{1}{\sqrt{h}} (-h_{12}p_u + h_{11}p_w) \right]_w \right\} \right. \\
& \quad \left. + (H^2 - K)p \right\} . \tag{9}
\end{aligned}$$

In conditions (8) and (9), H , K denote the mean and Gaussian curvatures of the boundary, respectively, γ is a stability parameter that depends on the wave velocity c and a curvature measure of the artificial boundary [21, 22], and h_{ij} ($i, j = 1, 2$) and h denote the components of the Euclidean metric tensor on the boundary Γ_a . We remark that Γ_a is oriented such that $H < 0, \forall \mathbf{x} \in \Gamma_a$; notice also that $K > 0, \forall \mathbf{x} \in \Gamma_a$, since Γ_a is convex by definition⁴.

Conditions (8) and (9) are written for an arbitrarily-shaped convex boundary; for the particular case of an ellipsoidal boundary, the various geometric measures introduced in (8)–(9), reduce to:

$$\begin{aligned}
h_{11} &= a^2 \cos^2 \theta \cos^2 \phi + b^2 \sin^2 \theta \cos^2 \phi + d^2 \sin^2 \phi, \\
h_{22} &= (a^2 \sin^2 \theta + b^2 \cos^2 \theta) \sin^2 \phi, \\
h_{12} &= (b^2 - a^2) \sin \theta \cos \theta \sin \phi \cos \phi, \\
h &= [a^2 b^2 \cos^2 \phi \\
& \quad + d^2 \sin^2 \phi (a^2 \sin^2 \theta + b^2 \cos^2 \theta)] \sin^2 \phi, \\
J &= [a^2 b^2 + [d^2 (a^2 - b^2) \sin^2 \theta - b^2 (a^2 - d^2)] \sin^2 \phi], \\
K &= \left(\frac{abd}{J} \right)^2, \\
H &= -\frac{abd}{2J^{\frac{3}{2}}} \\
& \quad \times [a^2 + b^2 + [(a^2 - b^2) \\
& \quad \times \sin^2 \theta - (a^2 - d^2)] \sin^2 \phi], \tag{10}
\end{aligned}$$

where the following surface parameterization was used (Fig. 2):

$$\begin{aligned}
x &= a \cos \theta \sin \phi, \\
y &= b \sin \theta \sin \phi, \\
z &= d \cos \phi, \text{ with } \phi \in [0, \pi] \text{ and } \theta \in [0, 2\pi], \tag{11}
\end{aligned}$$

and noting that $u \equiv \phi$ and $w \equiv \theta$ in (8) and (9). Equations (8) and (9), with the definitions (10), are the desired second-order absorbing boundary conditions suitable for ellipsoidal truncation geometries of interest herein. We remark that (9) can also be used for mixed geometries, e.g., a closed-cylinder boundary, or

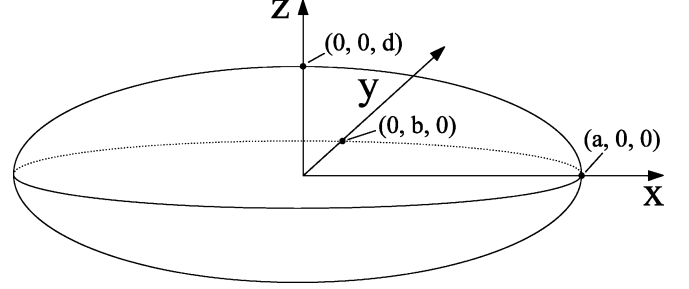


Fig. 2 Ellipsoidal absorbing boundary geometry

a box, etc, where the various geometric quantities in (8) and (9) need be appropriately modified. Whereas, depending on the boundary surface, curvature terms may vanish (e.g., for plane segments), invariably the tangential derivative terms survive. A mixed-geometry or box-type shape may allow for tighter circumscription of elongated scatterers; herein, notwithstanding the wider applicability of (8) and (9), we report only on ellipsoidal/spheroidal boundaries.

4 Finite element implementation

To set the stage for the numerical experiments we revisit next the key steps outlined in [21] and particularize to the ellipsoidal truncation geometry.

4.1 Semi-discrete form

In order to arrive at the semi-discrete forms valid for Ω_a using finite elements, we return to the strong statement (1), in order to recast it into a weak form. Notice, that the infinite domain Ω in (1) will now be replaced by the finite annular region Ω_a . Following classical lines, the weak statement can be cast as:

$$\begin{aligned}
\frac{1}{c^2} \int_{\Omega_a} \delta p \ddot{p} d\Omega_a + \int_{\Omega_a} \nabla \delta p \cdot \nabla p d\Omega_a \\
- \int_{\Gamma_a} \delta p p_v d\Gamma_a = - \int_{\Gamma} f_N \delta p d\Gamma . \tag{12}
\end{aligned}$$

The goal now is to replace p_v in (12) with the local approximant \mathcal{F}_2 given by either (8) (in the frequency-domain), or by (9) (in the time-domain). Notice, however, that as argued in [21], (9) needs further treatment, since it involves both the normal derivative of the pressure p_v and its first time derivative \dot{p}_v . In [21] we introduced auxiliary variables on Γ_a that allowed the decomposition of (9) and its ready incorporation into the weak form (12). Accordingly, let $q^{(1)}$ and $q^{(2)}$ denote the auxiliary variables on Γ_a . Then, one can show via Laplace transforms in time that the following set of three equations is equivalent to (9):

$$-p_v = \frac{1}{c}\dot{p} - Hp - \frac{c}{2\gamma} \mathcal{J} q^{(1)} - \frac{c}{2\gamma} (H^2 - K) q^{(2)}, \tag{13}$$

⁴Also, $(H^2 - K) \geq 0, \forall \mathbf{x} \in \Gamma_a$.

$$\mathcal{J}p - \mathcal{J}q^{(1)} - \frac{1}{\gamma}\mathcal{J}\dot{q}^{(1)} = 0 , \quad (14)$$

$$p - q^{(2)} - \frac{1}{\gamma}\dot{q}^{(2)} = 0 . \quad (15)$$

Here \mathcal{J} is the (Beltrami) differential operator defined by:

$$\mathcal{J}\cdot = \frac{1}{\sqrt{h}} \left\{ \left[\frac{1}{\sqrt{h}} (h_{22}(\cdot)_u - h_{12}(\cdot)_w) \right]_u + \left[\frac{1}{\sqrt{h}} (-h_{12}(\cdot)_u + h_{11}(\cdot)_w) \right]_w \right\} . \quad (16)$$

Next, we multiply (13) by δp , (14) by $\delta q^{(1)}$, and (15) by $\delta q^{(2)}$, where $\delta q^{(1)}$ and $\delta q^{(2)}$ are appropriate test functions and integrate by parts the terms associated with the operator \mathcal{J} . There results:

$$\begin{aligned} - \int_{\Gamma_a} \delta p p_v d\Gamma_a &= \frac{1}{c} \int_{\Gamma_a} \delta p p d\Gamma_a - \int_{\Gamma_a} H \delta p p d\Gamma_a \\ &+ \frac{c}{2} \int_{\Gamma_a} \frac{1}{\gamma} \nabla^s \delta p \cdot \nabla^s q^{(1)} d\Gamma_a \\ &- \frac{c}{2} \int_{\Gamma_a} \frac{1}{\gamma} (H^2 - K) \delta p q^{(2)} d\Gamma_a , \end{aligned} \quad (17)$$

$$\begin{aligned} &\frac{c}{2} \int_{\Gamma_a} \frac{1}{\gamma} \nabla^s \delta q^{(1)} \cdot \nabla^s p d\Gamma_a \\ &- \frac{c}{2} \int_{\Gamma_a} \frac{1}{\gamma} \nabla^s \delta q^{(1)} \cdot \nabla^s q^{(1)} d\Gamma_a \\ &- \frac{c}{2} \int_{\Gamma_a} \frac{1}{\gamma^2} \nabla^s \delta q^{(1)} \cdot \nabla^s \dot{q}^{(1)} d\Gamma_a = 0 , \quad (18) \\ &- \frac{c}{2} \int_{\Gamma_a} \frac{1}{\gamma} (H^2 - K) \delta q^{(2)} p d\Gamma_a \\ &+ \frac{c}{2} \int_{\Gamma_a} \frac{1}{\gamma} (H^2 - K) \delta q^{(2)} q^{(2)} d\Gamma_a \\ &+ \frac{c}{2} \int_{\Gamma_a} \frac{1}{\gamma^2} (H^2 - K) \delta q^{(2)} \dot{q}^{(2)} d\Gamma_a = 0 , \quad (19) \end{aligned}$$

in which ∇^s is the surface gradient on Γ_a defined as:

$$\begin{aligned} \nabla^s(\cdot) &= \frac{1}{h} (h_{22}(\cdot)_u - h_{12}(\cdot)_w) \mathbf{X}_u \\ &+ \frac{1}{h} (-h_{12}(\cdot)_u + h_{11}(\cdot)_w) \mathbf{X}_w . \end{aligned} \quad (20)$$

In addition, $q^{(1)}$ and $q^{(2)}$ are required to vanish at $t = 0$. Equations (17)–(19) can then be used to complete the weak-form formulation: the right side of (17) replaces the third term in (12), and (18) and (19) are added to the resulting modified weak form. We remark that with the decomposition (17)–(19), (12) will lead, upon spatial discretization, to a symmetric system of ordinary differential equations, in both the frequency- and

time-domains. In other words, the contributions from the absorbing boundary maintain both the symmetric structure of the interior problem and the sparsity of the associated system matrices.

4.2 System matrices

We use standard finite element isoparametric elements for approximating the geometry and for the spatial discretization of the pressure p in Ω_a and on Γ_a and of the auxiliary pressures $q^{(1)}$ and $q^{(2)}$ on Γ_a . Notice that the presence of first-order derivatives in (17)–(19) increases the usual smoothness requirements on the artificial boundary; in short, we seek p and δp that belong to $H^1(\Omega_a) \times H^1(\Gamma_a)$ where H^1 denotes the Sobolev space of degree 1. Similarly, $q^{(1)}$ and $\delta q^{(1)}$ need also belong to $H^1(\Gamma_a)$. We introduce:

$$p(\mathbf{x}, t) = \psi_1^T(\mathbf{x}) \mathbf{p}(t), \delta p(\mathbf{x}) = \delta \mathbf{p}^T \psi_1(\mathbf{x}) , \quad (21)$$

$$q^{(1)}(\mathbf{x}, t) = \psi_2^T(\mathbf{x}) \mathbf{q}^{(1)}(t), \delta q^{(1)}(\mathbf{x}) = \delta \mathbf{q}^{(1)T} \psi_2(\mathbf{x}) , \quad (22)$$

$$q^{(2)}(\mathbf{x}, t) = \psi_3^T(\mathbf{x}) \mathbf{q}^{(2)}(t), \delta q^{(2)}(\mathbf{x}) = \delta \mathbf{q}^{(2)T} \psi_3(\mathbf{x}) , \quad (23)$$

in which, ψ_1 , ψ_2 and ψ_3 are vectors of shape functions and \mathbf{p} , $\mathbf{q}^{(1)}$ and $\mathbf{q}^{(2)}$ are vector fields of the unknown nodal functions in time. Substitution of (21)–(23) into (12) and (17)–(19) results in a system of ordinary differential equations with the following classical second-order structure:

$$\mathbf{M}\ddot{\mathbf{P}}(t) + \mathbf{C}\dot{\mathbf{P}}(t) + \mathbf{K}\mathbf{P}(t) = \mathbf{F}(t) , \quad (24)$$

where, $\mathbf{P}^T = [\mathbf{p}_\Gamma^T, \mathbf{p}_{\Omega_a}^T, \mathbf{p}_{\Gamma_a}^T, \mathbf{q}^{(1)T}, \mathbf{q}^{(2)T}]$ and \mathbf{p}_Γ , \mathbf{p}_{Ω_a} , \mathbf{p}_{Γ_a} denote partitions of \mathbf{p} over Γ , Ω_a , and Γ_a , respectively; \mathbf{M} , \mathbf{C} and \mathbf{K} are the mass, damping and stiffness matrices of the system, and \mathbf{F} denotes the excitation. The matrices \mathbf{M} , \mathbf{C} and \mathbf{K} have the following form:

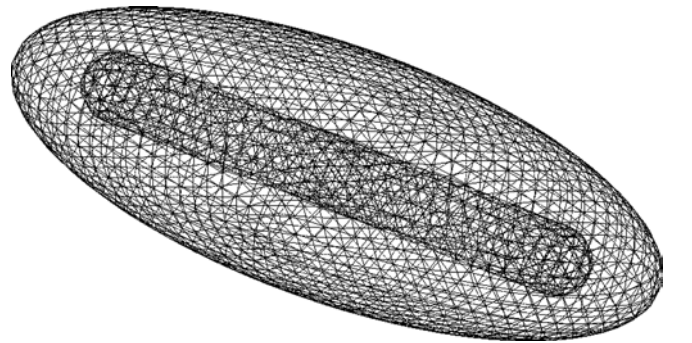


Fig. 3 Typical tetrahedral mesh over the bounded computational domain Ω_a ; shown are the element traces on the absorbing boundary and the scatterer surface

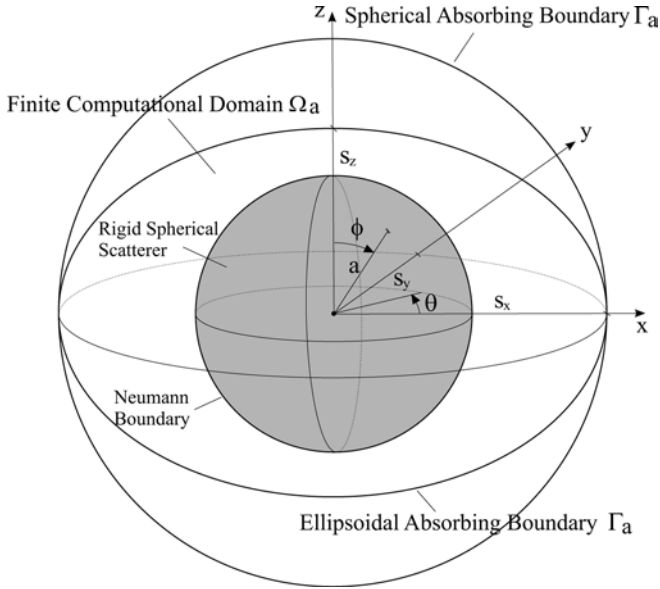


Fig. 4 Model of rigid scatterer surrounded by an absorbing boundary

$$\mathbf{M} = \begin{bmatrix} M_{p\Gamma p\Gamma}^f & M_{p\Gamma p\Omega_a}^f & 0 & 0 & 0 \\ M_{p\Omega_a p\Gamma}^f & M_{p\Omega_a p\Omega_a}^f & M_{p\Omega_a p\Gamma_a}^f & 0 & 0 \\ 0 & M_{p\Gamma_a p\Omega_a}^f & M_{p\Gamma_a p\Gamma_a}^f & 0 & 0 \\ 0 & 0 & 0 & 0 & 0 \\ 0 & 0 & 0 & 0 & 0 \end{bmatrix}, \quad (25)$$

$$\mathbf{C} = \begin{bmatrix} 0 & 0 & 0 & 0 & 0 \\ 0 & 0 & 0 & 0 & 0 \\ 0 & 0 & C_{p\Gamma_a p\Gamma_a}^a & 0 & 0 \\ 0 & 0 & 0 & C_{q^{(1)} q^{(1)}}^a & 0 \\ 0 & 0 & 0 & 0 & C_{q^{(2)} q^{(2)}}^a \end{bmatrix}, \quad (26)$$

$$\mathbf{K} = \begin{bmatrix} K_{p\Gamma p\Gamma}^f & K_{p\Gamma p\Omega_a}^f & 0 & 0 & 0 \\ K_{p\Omega_a p\Gamma}^f & K_{p\Omega_a p\Omega_a}^f & K_{p\Omega_a p\Gamma_a}^f & 0 & 0 \\ 0 & K_{p\Gamma_a p\Omega_a}^f & K_{p\Gamma_a p\Gamma_a}^f + K_{p\Gamma_a p\Gamma_a}^a & K_{p\Gamma_a q^{(1)}}^a & K_{p\Gamma_a q^{(2)}}^a \\ 0 & 0 & K_{q^{(1)} p\Gamma_a}^a & K_{q^{(1)} q^{(1)}}^a & 0 \\ 0 & 0 & K_{q^{(2)} p\Gamma_a}^a & 0 & K_{q^{(2)} q^{(2)}}^a \\ 0 & 0 & & & \end{bmatrix}. \quad (27)$$

As it can be seen from (25)–(27), the top left blocks are the standard mass and stiffness matrices associated with the fluid (superscript f), and the bottom right blocks represent, respectively, the effective damping and stiffness introduced by the absorbing boundary

(superscript a). Notice that there is no inertia associated with our approximate absorbing boundary and that the only damping in the system comes from the absorbing boundary which is associated with the radiated energy in the actual unbounded system. Finally, the forcing vector \mathbf{F} in (24) is given as:

$$\mathbf{F}^T = [\mathbf{F}_N^T, 0^T, 0^T, 0^T, 0^T],$$

$$\text{with } \mathbf{F}_N = - \int_{\Gamma} f_N \psi_1 d\Gamma.$$

4.3 Element matrices

Since \mathbf{C}^a and \mathbf{K}^a in (26) and (27) are local and symmetric, they can be constructed element by element and incorporated into the equations of motion by standard assembly techniques using existing finite element software. All that is necessary is to incorporate the corresponding element matrices \mathbf{c}^a and \mathbf{k}^a into the finite element library of any existing software package for interior problems. The element matrices \mathbf{k}^a and \mathbf{c}^a are given as:

Table 1 Relative $L_2(\Gamma)$ errors (E) in percent for $\mathbf{ka} = 1$

| Boundary Shape | Ellipsoid | Prolate Spheroid | Sphere | |
|-------------------|-----------|------------------|--------|--------|
| $S_x : S_y : S_z$ | 3:2:1.5 | 3:2:2 | 3:3:3 | |
| DOF | 37872 | 50636 | 91138 | |
| $n = 0$ | $m = 0$ | 0.8422 | 0.5355 | 0.3945 |
| $n = 1$ | $m = 0$ | 1.5315 | 1.3608 | 1.2393 |
| $n = 1$ | $m = 1$ | 1.1909 | 1.4208 | 1.1976 |
| $n = 2$ | $m = 0$ | 3.1995 | 2.9018 | 2.5407 |
| $n = 2$ | $m = 1$ | 2.2802 | 2.7782 | 2.5387 |
| $n = 2$ | $m = 2$ | 3.0689 | 3.5767 | 2.5455 |
| $n = 3$ | $m = 0$ | 6.7732 | 5.7986 | 3.9113 |
| $n = 3$ | $m = 1$ | 6.4525 | 5.8156 | 3.8641 |
| $n = 3$ | $m = 2$ | 6.4559 | 6.4001 | 3.9757 |
| $n = 3$ | $m = 3$ | 6.6228 | 6.7067 | 3.9882 |

Table 2 Relative $L_2(\Gamma)$ errors (E) in percent for $\mathbf{ka} = 5$

| Boundary Shape | Ellipsoid | Prolate Spheroid | Sphere | |
|-------------------|-----------|------------------|--------|--------|
| $S_x : S_y : S_z$ | 3:2:1.5 | 3:2:2 | 3:3:3 | |
| DOF | 37872 | 50636 | 91138 | |
| $n = 0$ | $m = 0$ | 2.9756 | 3.3767 | 1.2395 |
| $n = 1$ | $m = 0$ | 2.1816 | 2.8964 | 1.2621 |
| $n = 1$ | $m = 1$ | 3.0025 | 3.3346 | 1.2378 |
| $n = 2$ | $m = 0$ | 2.6664 | 2.2713 | 1.3868 |
| $n = 2$ | $m = 1$ | 2.0696 | 2.3027 | 1.7639 |
| $n = 2$ | $m = 2$ | 2.0950 | 2.5630 | 1.5205 |
| $n = 3$ | $m = 0$ | 2.9083 | 2.5435 | 1.9721 |
| $n = 3$ | $m = 1$ | 3.2518 | 2.9509 | 1.8849 |
| $n = 3$ | $m = 2$ | 3.5907 | 3.7041 | 2.0487 |
| $n = 3$ | $m = 3$ | 3.4565 | 3.8703 | 1.7824 |

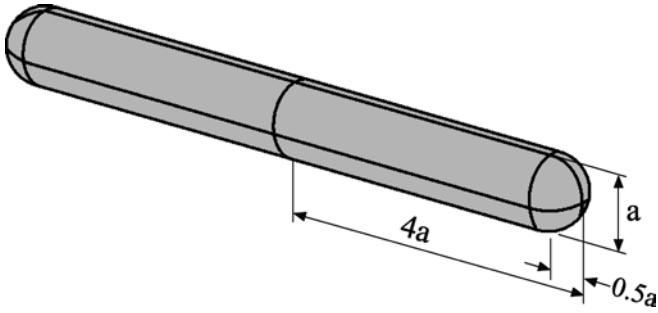


Fig. 5 Geometry of elongated scatterer; dimensional ratio along the median axes is 8:1:1

$$\mathbf{k}^a = \frac{c}{2} \begin{bmatrix} \frac{2}{c} \mathbf{k}_{11} & \mathbf{k}_{12} & -\mathbf{k}_{13} \\ \mathbf{k}_{12}^T & -\mathbf{k}_{22} & 0 \\ -\mathbf{k}_{13}^T & 0 & \mathbf{k}_{33} \end{bmatrix},$$

$$\mathbf{c}^a = \frac{c}{2} \begin{bmatrix} \frac{2}{c^2} \mathbf{c}_{11} & 0 & 0 \\ 0 & -\mathbf{c}_{22} & 0 \\ 0 & 0 & \mathbf{c}_{33} \end{bmatrix}, \quad (29)$$

with the following definitions for the individual matrices:

$$\begin{aligned} \mathbf{k}_{11} &= - \int_{\Gamma_a^e} H \psi_1 \psi_1^T d\Gamma_a^e, \\ \mathbf{k}_{22} &= \int_{\Gamma_a^e} \frac{1}{\nabla^s} \psi_2 \cdot \nabla^s \psi_2^T d\Gamma_a^e, \\ \mathbf{k}_{33} &= \int_{\Gamma_a^e} \frac{1}{(H^2 - K)} \psi_3 \psi_3^T d\Gamma_a^e, \\ \mathbf{k}_{12} &= \int_{\Gamma_a^e} \frac{1}{\nabla^s} \psi_1 \cdot \nabla^s \psi_2^T d\Gamma_a^e, \\ \mathbf{k}_{13} &= \int_{\Gamma_a^e} \frac{1}{(H^2 - K)} \psi_1 \psi_3^T d\Gamma_a^e, \\ \mathbf{c}_{11} &= \int_{\Gamma_a^e} \psi_1 \psi_1^T d\Gamma_a^e, \\ \mathbf{c}_{22} &= \int_{\Gamma_a^e} \frac{1}{\nabla^s} \psi_2 \cdot \nabla^s \psi_2^T d\Gamma_a^e, \\ \mathbf{c}_{33} &= \int_{\Gamma_a^e} \frac{1}{\nabla^s} (H^2 - K) \psi_3 \psi_3^T d\Gamma_a^e, \end{aligned} \quad (30)$$

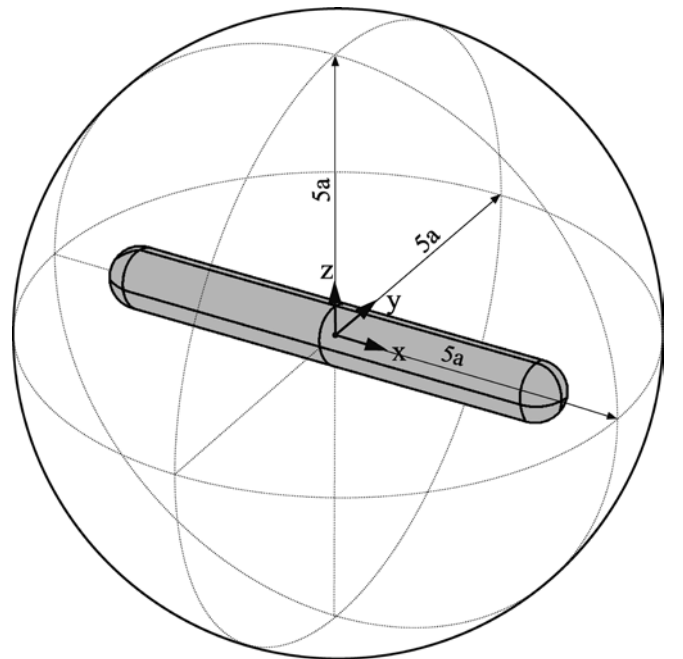
where $d\Gamma_a^e$ and the operator ∇^s denote the area differential and the approximation of the surface gradient ∇^s (or (20)) on an element Γ_a^e of Γ_a , respectively. Notice that the element defined by (29) is a surface-only element.

We remark that, as it can be seen from (30), the element matrices characterizing the absorbing element

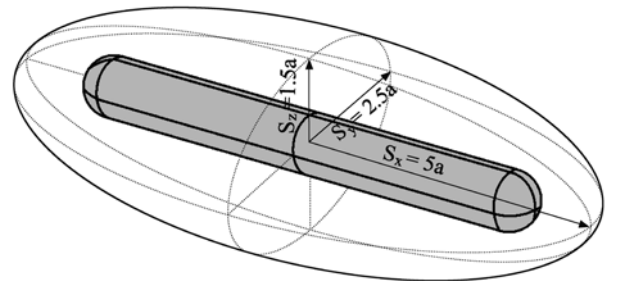
implicate integrands that include expressions of the two curvature measures (Gaussian K , and mean H curvature) of the boundary. Whereas the geometry of the boundary is approximated piecewise (isoparametric elements), by low-order surfaces (e.g., planes), we have chosen to use the exact expressions (10) for the curvatures. This choice introduces a discrepancy since the curvatures refer to boundary segments not represented by the isoparametric description; however, the error introduced by the mismatch is of order higher than

Table 3 Wave incidence vectors

| Incidence index | Incidence vector ($\alpha_x, \alpha_y, \alpha_z$) |
|-----------------|---|
| P_{i_x} | (0°, 90°, 90°) |
| P_{i_y} | (90°, 0°, 90°) |
| P_{i_z} | (90°, 90°, 0°) |
| $P_{i_{25}}$ | (125.26°, 125.26°, 125.26°) |



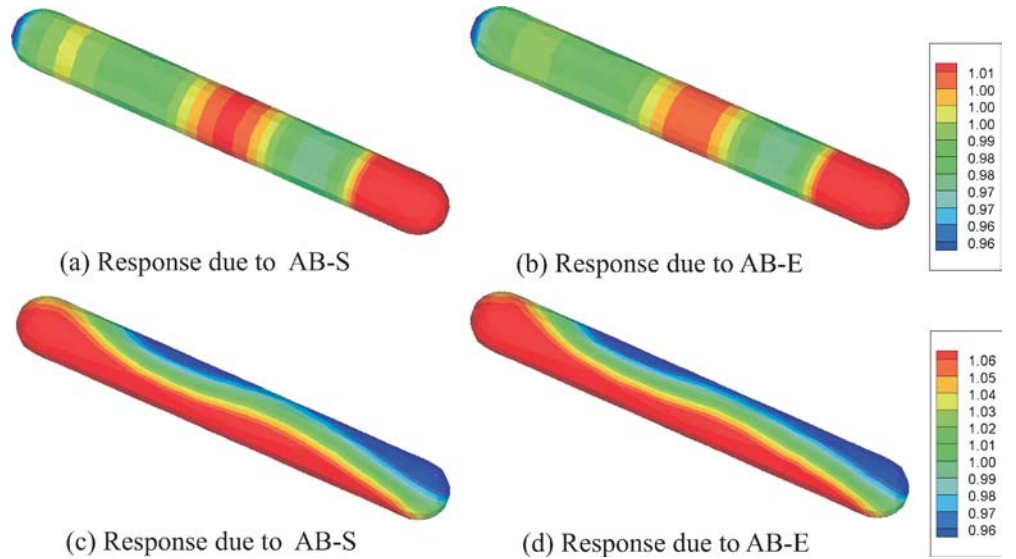
(a) Spherical boundary (radius = 5a)



(b) Ellipsoidal boundary ($S_x:S_y:S_z=5:2.5:1.5$)

Fig. 6a, b Geometry of absorbing boundaries for finite cylinder problem

Fig. 7a–d Amplitude of total pressure; cases **a** and **b** due to head-on incidence (\mathbf{P}_{i_x}); cases **c** and **d** due to oblique incidence ($\mathbf{P}_{i_{25}}$)



the approximation error, does not dominate, and can thus be safely neglected.

5 Numerical experiments

The second-order condition (8) (or (9)) was implemented on ellipsoidally-shaped boundaries, as per the details of the preceding section. We implemented trilinear 8-noded elements for the discretization of the finite domain Ω_a , and 4-noded bilinear quadrilaterals for the absorbing boundary elements on Γ_a ; however, for all results presented here, we used unstructured tetrahedral meshes and triangularly-shaped surface elements on the absorbing boundary (Fig. 3). The tetrahedral and triangular elements were obtained as degenerate cases of the trilinear hexahedral and bilinear

Table 4 Computational cost in terms of number of degree-of-freedom per type of absorbing boundary

| Types of absorbing boundary | | $S_x : S_y : S_z$ | DOF |
|-----------------------------|----------------------|-------------------|--------|
| Reference (spherical) | | 8:8:8 | 201692 |
| AB-S | Spherical | 5:5:5 | 50016 |
| AB-PS1 | Prolate spheroidal 1 | 5:3:3 | 23774 |
| AB-PS2 | Prolate spheroidal 2 | 5:1.5:1.5 | 7262 |
| AB-E | Ellipsoidal | 5:2.5:1.5 | 11374 |

Table 5 Relative L_2 errors (\mathbf{E}) in percent for $\mathbf{ka} = \mathbf{1}$

| Incidence index | AB-S | AB-PS1 | AB-E | AB-PS2 |
|-----------------|--------|--------|--------|--------|
| P_{i_x} | 2.6459 | 2.8439 | 5.3357 | 7.0457 |
| P_{i_y} | 2.2093 | 2.5848 | 3.2001 | 3.3657 |
| P_{i_z} | 2.4309 | 2.4429 | 3.0799 | 3.7976 |
| $P_{i_{25}}$ | 1.3816 | 1.3838 | 2.0062 | 2.2500 |

quadrilateral elements we implemented. Furthermore, we used $\psi_1 = \psi_2 = \psi_3$. Numerical experiments to assess the performance of the condition and the associated discrete forms (absorbing element (29)) have been conducted for both radiation and scattering problems in the frequency- and time-domains. We report here on a subset of our numerical experiments. Throughout all problems we used:

$$\gamma = -cH, \quad (31)$$

for the stability parameter γ in (8)–(9). With this choice the stability criterion for time-domain calculations established in [21] is satisfied.⁵

All numerical results reported herein were obtained using a sequential implementation for constructing the various matrices, and a parallel implementation for solving the resulting algebraic systems. For the latter we used MPICH (Argonne National Laboratories) for the message passing interface, and a solver from the suite of Krylov-subspace methods available through PETSc [28] on a 4-processor Ultra-80 symmetric multiprocessor system.

5.1 Radiation problems – frequency-domain

To assess the performance of the boundaries we consider first the radiation problem arising from prescribing an acceleration field on the surface of a spherical scatterer (Fig. 4) of radius a ; specifically, let:

$$p_r = \rho A_0 P_n^{(m)}(\cos \phi) \cos m\theta e^{i\omega t}, \quad \text{at } r = a, \quad (32)$$

⁵In [21] we had shown that a necessary condition for stability is that $\gamma \geq \gamma_{cr} = \frac{c}{2} \left(-\frac{H^2 - K}{H} \right)_{\max}$; with $\gamma = -cH$, and the assertions $H < 0$, $K > 0$, $\forall \mathbf{x} \in \Gamma_a$, the stability criterion leads to $H^2 + K > 0$.

where p_r denotes radial pressure derivative, ρ denotes the surrounding fluid's density, A_0 is the amplitude of the prescribed field, θ is the meridional angle, ϕ is the polar angle, n, m denote the order of the tesseral harmonics, $P_n^{(m)}$ is the associated Legendre function of the first kind, degree n , and order m , and ω is the driving circular frequency. In this case, the exact solution for the radiated field in the domain exterior to the scatterer ($r \geq a$) is:

$$p_{\text{ex}}(r, \theta, \phi) = \rho A_0 R_i \frac{h_n^{(2)}(kr)}{n h_n^{(2)}(ka) - ka h_{n+1}^{(2)}(ka)} \times P_n^{(m)}(\cos \phi) \cos m\theta, \quad (33)$$

where $h_n^{(2)}$ is the spherical Hankel function of the second kind and of n -th order; in (33), k denotes wavenumber ($k = \omega/c$).

We surround the spherical cavity with co-centric ellipsoids of various sizes and semi-axes values and solve the boundary value problem in Ω_a using the second-order condition on Γ_a (Fig. 4). We measure the relative error using L_2 -norms on the scatterer's boundary Γ as:

$$E = \frac{\left[\int_{\Gamma} \|p_{\text{ex}} - p_{\text{app}}\|^2 d\Gamma \right]^{\frac{1}{2}}}{\left[\int_{\Gamma} \|p_{\text{ex}}\|^2 d\Gamma \right]^{\frac{1}{2}}} \times 100\%, \quad (34)$$

where p_{app} is the approximate solution obtained by solving (24) in the frequency-domain.

Denoting the ellipsoid's semi-axes with S_x, S_y , and S_z , respectively, (Fig. 4), Tables 1 and 2 summarize the errors associated with the prototype radiation problem for a relatively low frequency $ka = 1$, and a medium frequency $ka = 5$, respectively, and for three different absorbing boundaries: an ellipsoid, a prolate spheroid, and a sphere. Shown also is the computational cost in terms of the total number of degrees-of-freedom. The typical mesh size for all cases was $0.12a$. With the exception of the higher modes (e.g., $n = 3$ and $ka = 1$) the performance of the ellipsoidal and spheroidal boundaries is comparable, in terms of accuracy (error levels), to the spherical boundary, at a substantial reduction of the computational cost (by nearly 60%). However, even though there are cases (e.g., $n = 2, m = 1$ in Table 1) where the errors associated with the ellipsoidal are less than those of the spherical boundary, the overall trend is that the spherical boundary results in smaller errors, albeit at increased computational cost. We remark though that the results are sensitive to the quality of the mesh: we have observed deterioration of the accuracy for the higher modes when using the ellipsoidal boundary due to numerical dispersion, while still using the same mesh density as with the spherical boundary⁶. In other words, the errors reported in Tables 1 and 2 include the total discretization error (due to both the geometry and the solution approximations), the dispersion error, and the error introduced by the use of the approximant to the exact boundary condition. The dispersion error is a significant part of the total error, and dominates in the case of the non-spherical geometries; this is so, since it is easy to create a radially-aligned mesh (and thus minimize dispersion error) in the case of the spherical annulus; by contrast, we used highly unstructured meshes for all other cases (see Fig. 3). Hence, the reported errors tend to unduly favor the spherical boundaries.

We further remark that, by construction [21], we expect the boundaries to perform quite well at the medium to high frequency range, and exhibit poor accuracy at the low end of the spectrum (e.g., $ka < 0.5$), and particularly so for near-static cases. However, as it can be seen from Table 1, the performance, even at the lower end, is still quite satisfactory. Notice also that the smallest distance from the scatterer to the absorbing boundary for the reported radiation problems is only a small fraction of the dominant wavelength: the distance from the "north pole" of the scatterer (Fig. 4) to the absorbing boundary is $0.5a$, when the wavelength for

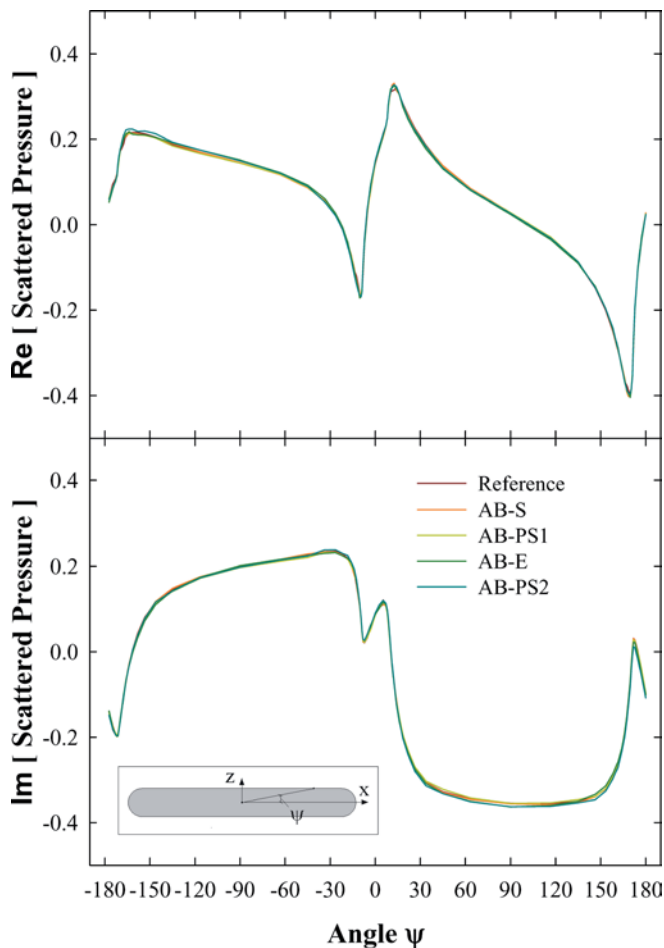
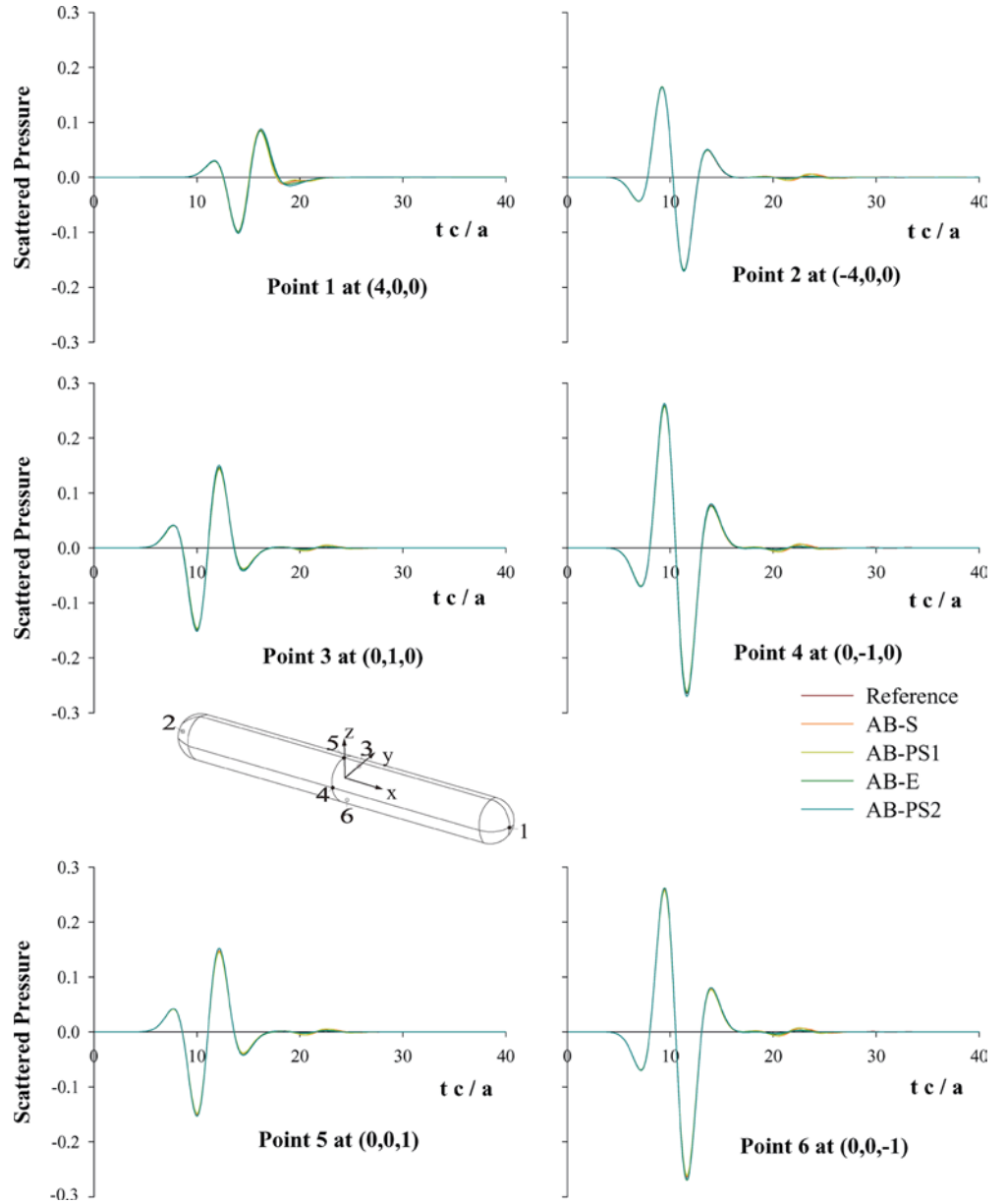


Fig. 8 Real and imaginary parts of scattered pressure on the surface of the scatterer along the xz -plane due to oblique incidence (\mathbf{P}_{i25})

⁶Dispersion is not addressed here, since no special schemes have been implemented to alleviate the dispersion error.

Fig. 9 Normalized scattered pressure traces; transient response to a traveling plane wave (Ricker pulse)



$ka = 1$ is $2\pi a$. That is, the boundary is, approximately, 0.08 wavelengths away from the scatterer. Whereas, such a close placement may be too tight for applications, we believe that, based on numerical experiments not reported herein, satisfactory results can be obtained with boundaries placed at 0.2 of the dominant wavelength (still at only a fraction of a wavelength).

5.2 Scattering problems – frequency-domain

The computational savings are expected to be greater in the presence of elongated scatterers, where an ellipsoidal boundary can offer a tighter circumscription of the insonified obstacle. To this end, we discuss the response of a rigid finite cylinder (Fig. 5; the cylinder is terminated

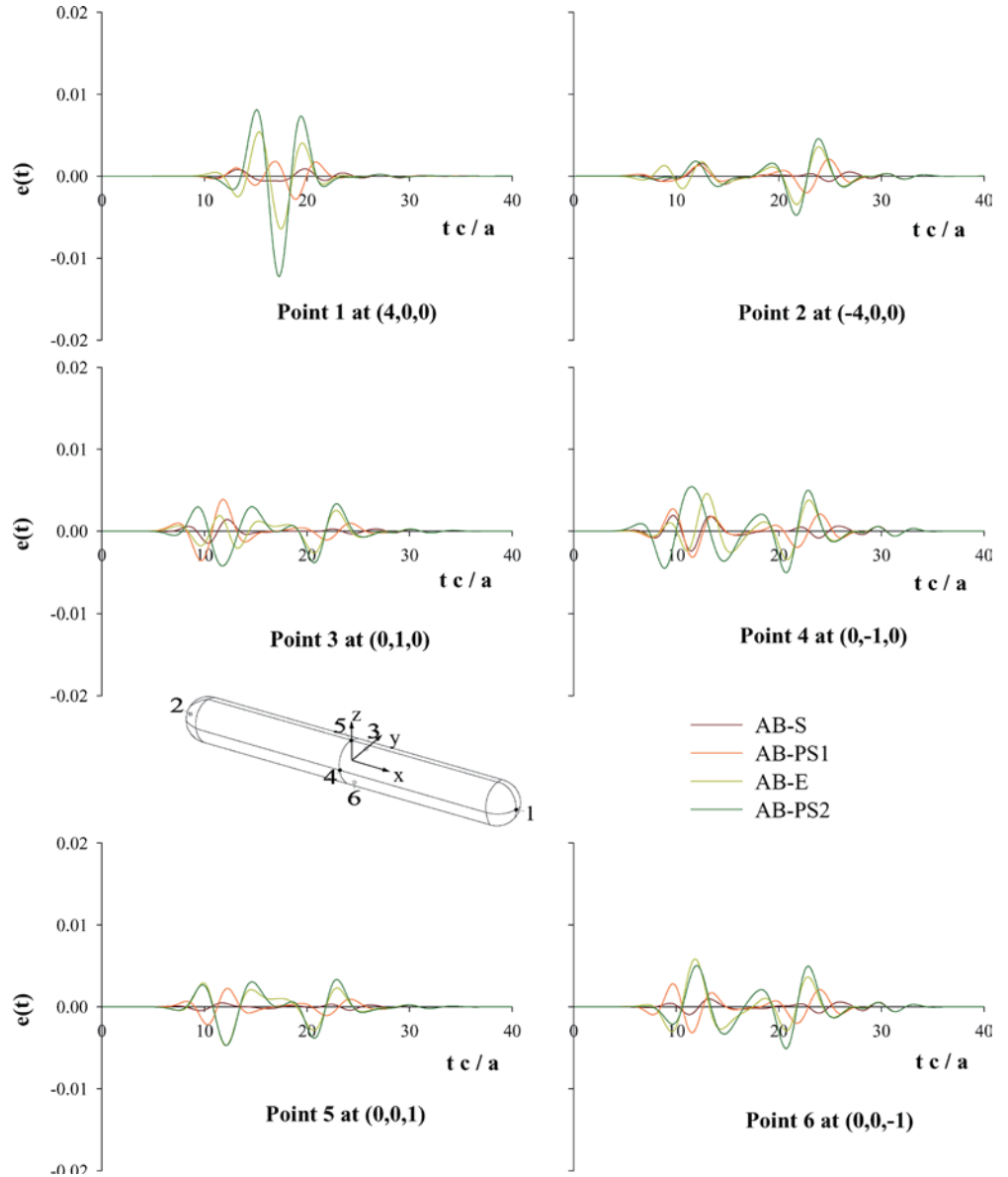
with two semi-spherical caps) to four different cases of an incoming plane wave impinging on the scatterer at different angles of incidence. Specifically, we prescribe the incident plane wave of unit amplitude:

$$P^{\text{inc}} = e^{-ik(x \cos \alpha_x + y \cos \alpha_y + z \cos \alpha_z)} e^{i\omega t}, \quad (35)$$

where α_x , α_y , and α_z are the angles formed between the normal to the traveling wave front and the three coordinate axes. We considered four cases of incidence corresponding to the sets indicated in Table 3 and a single frequency ($ka = 1$).

We surround the cylinder with four different absorbing boundaries, that is, a sphere, two different prolate spheroids, and an ellipsoid, as depicted in Fig. 6 and Table 4; the characteristic mesh metric was $0.25a$. Since in these cases there is no exact solution to compare

Fig. 10 Traces of error $e(t)$; transient response to a traveling plane wave (Ricker pulse)



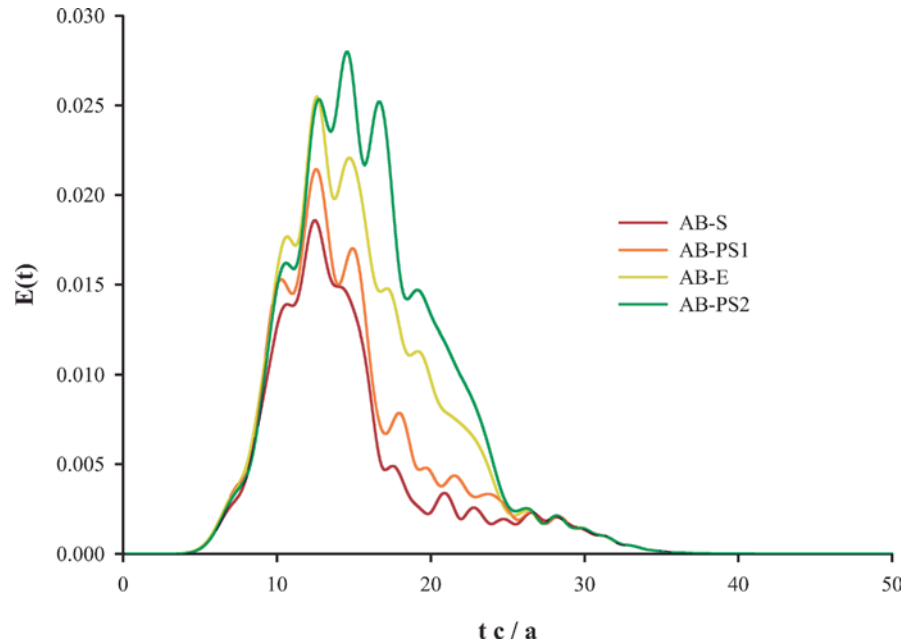
against we create a reference solution by placing a spherical absorbing boundary at a distance of $8a$ (Table 4), also endowed with a second-order condition (we use the same mesh density). We measure errors again in the L_2 -norm, defined in (34), with respect to this reference solution. Table 5 summarizes the errors on the surface of the scatterer. Figure 7 depicts the distribution of the total pressure on the surface of the scatterer for two out of the four incidence cases (P_{i_x} and $P_{i_{125}}$) and for two absorbing boundary surfaces (AB-S and AB-E). Figure 8 depicts the variation of the normalized real and imaginary parts of the scattered pressure along the xz -plane on the surface of the scatterer for the case of oblique incidence for all four absorbing boundaries. It is clear that the agreement is excellent. Notice further that, while in all cases, the spherical boundary performs better when compared against the reference solution (Table 5),

the gain in accuracy is marginal in all cases with the exception of AB-PS2 for which the circumscription is very tight. It is thus important to observe that, for example, AB-PS1 offers essentially the same accuracy for less than 50% of the computational cost associated with the spherical boundary.

5.3 Scattering problems – time-domain

To illustrate the applicability of the absorbing elements to time-domain applications, Fig. 9 pertains to a direct time-domain solution of (24) for the scattered pressure field due to the insonification of the long cylinder by a traveling plane wave. To formally define the IBVP problem we set the normal derivative of the scattered pressure equal to the negative of the normal derivative

Fig. 11 L^2 -norm error $E(t)$



of the incident pressure on the scatterer's surface. We use the implicit trapezoidal rule to integrate in time the semi-discrete form (24) with a time step $\Delta t c/a = 0.1$. Finally, the time signal for the plane wave is given by a modified Ricker pulse with a peak central frequency ω_r . For the case shown in Fig. 9 we used $\omega_r a/c = 1$. In Fig. 9 depicted are the time traces of the scattered pressure at selected surface points on the scatterer. Figure 10 shows for the same problem the pointwise error $e(t) = p_{\text{ref}} - p_{\text{app}}$ between the reference solution p_{ref} and the approximate solution p_{app} –the latter obtained using each of the four different absorbing boundaries (spherical, 2 spheroidal, and ellipsoidal). Finally, Fig. 11 depicts the time-dependent L_2 -norm error $E(t) = (\int_{\Gamma} [p_{\text{ref}} - p_{\text{app}}]^2 d\Gamma)^{\frac{1}{2}}$ sampled on the surface of the scatterer, again for all four boundaries. The same behavior and features already identified in the frequency-domain characterize the response in time as well. The agreement between the reference solution and, the ellipsoidally-shaped boundaries are excellent (notice the small L_2 errors in Fig. 11).

6 Conclusions

In this article, we presented results pertaining to second-order absorbing boundary conditions prescribed on ellipsoidally-shaped boundaries for the three-dimensional numerical simulation of scalar wave propagation in either the time- or the frequency-domains. The local wave absorption properties of the condition depend on the curvatures of the truncation boundary, and terms accounting for the curvature variations appear explicitly in the developed conditions. We have shown the equivalence of the conditions, upon

discretization under a Galerkin scheme, to simple wave absorbing finite elements fully described by symmetric frequency-independent element matrices. Based on the obtained numerical results we conclude that significant computational savings are attainable by the use of the proposed ellipsoidally-shaped boundaries endowed with second-order conditions compared to the corresponding spherical boundaries. The savings, measured in the number of unknowns in the resulting algebraic system, are of the order of 50% – 80% over the spherical boundaries.

References

1. Antoine X, Barucq H, Bendali A (1999) Bayliss-Turkel radiation conditions on surfaces of arbitrary shape. *J. Math. Anal. Appl.* 229: 184–211
2. Astley RJ, Coyette J-P (2001) The performance of spheroidal infinite elements. *Int. J. Numer. Meth. Eng.* 52: 1379–1396
3. Astley RJ, Coyette J-P (2001) Conditioning of infinite element schemes for wave problems. *Commun. Numer. Meth. Eng.* 17: 31–41
4. Astley RJ (2000) Infinite elements for wave problems: a review of current formulations and an assessment of accuracy. *Int. J. Numer. Meth. Eng.* 49: 951–976
5. Astley RJ (1998) Transient spheroidal elements for unbounded wave problems. *Comput. Meth. Appl. Mech. Eng.* 164: 3–15
6. Astley RJ (1996) Transient wave envelope elements for wave problems. *J. Sound Vibration.* 192: 245–261
7. Astley RJ (1983) Wave envelope and infinite elements for acoustical radiation. *Int. J. Numer. Meth. Fluids* 88: 47–64
8. Bettess P (1977) Infinite elements. *Int. J. Numer. Meth. Eng.* 11: 53–64
9. Bettess P, Zienkiewicz OC (1977) Diffraction and refraction of surface waves using finite and infinite elements. *Int. J. Numer. Meth. Eng.* 11: 1271–1290
10. Bayliss A, Turkel E (1980) Radiation boundary conditions for wave-like equations. *Commun. Pure Appl. Math.*, 33(6): 707–725

11. Burnett DS (1994) A three-dimensional acoustic infinite element based on a prolate spheroidal multipole expansion. *J. Acoustical Society of America*. 96(5): 2798–2816
12. Burnett DS, Holford RL (1998) An ellipsoidal acoustic infinite element. *Comput. Meth. Appl. Mech. Eng.* 164: 49–76
13. Engquist B, Majda A (1977) Absorbing boundary conditions for numerical simulation of waves. *Math. Comput.* 31(139): 629–651
14. Engquist B, Majda A (1979) Radiation boundary conditions for acoustic and elastic wave calculations. *Commun. Pure Appl. Math.* 32(3): 313–357
15. Gerdes K, Demkowicz L (1996) Solution of 3D-Laplace and Helmholtz equations in exterior domains using hp-infinite elements. *Comput. Meth. Appl. Mech. Eng.* 137: 239–273
16. Givoli D (1999) Exact representations on artificial interfaces and applications in mechanics. *Appl. Mech. Reviews* 52(11): 333–349
17. Givoli D (1991) Non-reflecting boundary conditions: a review. *J. Comput. Phys.* 94(1): 1–29
18. Grote MJ, Keller JB (1995) On nonreflecting boundary conditions. *J. Comput. Phys.* 231–243
19. Hagstrom T (1999) Radiation boundary conditions for the numerical simulation of waves. *Acta Numer.* 47–106
20. Jones DS (1988) An approximate boundary condition in acoustics. *J. Sound Vibration* 121(1): 37–45
21. Kallivokas LF, Bielak J, MacCamy RC (1997) A simple impedance-infinite element for the finite element solution of the three-dimensional wave equation in unbounded domains. *Comput. Meth. Appl. Mech. Eng.* 147: 235–262
22. Kallivokas LF (1995) Absorbing boundary conditions and finite elements for transient and harmonic steady-state acoustic fluid-structure interaction. Thesis presented to Carnegie Mellon University in partial fulfillment of the requirements for the degree of Doctor of Philosophy, Pittsburgh
23. Kriegsmann GA, Taflove A, Umashankar KR (1987) A new formulation of electromagnetic wave scattering using an on-surface radiation boundary condition approach. *IEEE Trans. Antennas and Propagation*, AP-35(2): 153–160
24. Leis R (1986) *Initial Boundary Value Problems in Mathematical Physics*, John Wiley & Sons
25. Shirron JJ, Babuška I (1998) A comparison of approximate boundary conditions and infinite element methods for exterior Helmholtz problems. *Comput. Meth. Appl. Mech. Eng.* 164: 121–139
26. Tezaur R, Macedo A, Farhat C, Djellouli R (2002) Three-dimensional finite element calculations in acoustic scattering using arbitrarily shaped convex artificial boundaries. *Int. J. Numer. Meth. Eng.* 53: 1461–1476
27. Thompson LL, Huan R, Ianculescu C (1999) Finite element formulation of exact Dirichlet-to-Neumann radiation conditions on elliptic and spheroidal boundaries. *Proc. ASME Noise Control and Acoustics Division*. NCA-26: 497–509
28. Balay S, Buschelman K, Gropp WD, Kaushik D, Knepley M, McInnes LC, Smith BF, Zhang H (2002) *PETSc Users Manual*, ANL-95/11-Revision 2.1.5, Argonne National Laboratory